Detector for Spin-Filtering Experiment
Optimization and preformance

Gogi Macharashvili

1 Introduction

The PAX collaboration recently suggested to study the polarization build-up in an antiproton beam at the AD-ring of CERN at energies in the range of $50-200$ MeV [1]. The polarization build-up by spin filtering of stored antiprotons by multiple passage through a polarized internal hydrogen gas target gives a direct access to the spin dependence of the $\bar{p}p$ total cross section.

An important subject is the development of a detector system that allows one to efficiently determine the polarizations of beam and target. Such a system based on silicon microstrip detectors has recently been developed at IKP [2].

The main objective of recently proposed spin-filtering experiments at COSY [3] and AD-CERN [4] relate to physics of the polarization build-up in a stored proton (antiproton) beams. Two scenarios of stored beam polarization passing through polarized internal target exist. Understanding to which one is really work is crucial to progress towards the goal to produce stored antiproton beam. The polarized antiproton beam is the main necessary component to realize the PAX project [5].

The simulation study has been carried out in order to design and optimize a common detector to measure the polarization observables in pp and $\bar{p}p$ elastic scattering. The detector has to be optimized to detect the scattered particles in the energy range $40 < T_{p(\bar{p})} < 500\,MeV$. For the detector performance estimate we used Geant3 and Geant4 packages.

2 Primary interaction

In the primary $\bar{p}p$ interaction events sequence all branches are presented by default: $\bar{p}p \to \bar{p}p$, $\bar{p}p \to \bar{n}n$, $\bar{p}p \to X$, with partial probabilities shown in Table 1. The primary interaction is generated in 3 different ways:

(1) for $\bar{p}p \to \bar{p}p$ elastic scattering the Haidenbauer model [8] is used ($d\sigma/d\Omega$, A_y),

(2) for inelastic interaction secondaries generation the CHIPS model is used. The relative intensities of these reactions are taken also from [6] (see Fig.1) and are set equal (see Table 1) at all energies.

(3) for $\bar{p}p \to \bar{n}n$ charge exchange scattering the experimental data taken from [6] are used,

The reaction channels are distributed randomly in the event stream, so the stream structure is analogous to the real event stream accepted at measurement time.

Beam energy	MeV	43	120	220
Momentum	MeV/c	286	491	679
$\sqrt{s}$	MeV	1897.9	1935.6	1983.5
σ_{tot}	mb	250	175	145
elastic $\bar{p}p \to \bar{p}p$ (1)	%	33	33	33
inelastic $\bar{p}p \to X$ (2)	%	60	60	60
charge-exchange $\bar{p}p \to \bar{n}n$ (3)	%	7	7	7

Table 1. Primary interaction profile.

total cross-section

Total cross-section $\sigma_{tot}^{\bar{p}p}$ at the three energies have been taken from [6] (see Fig.1).

elastic scattering generation $\bar{p}p \to \bar{p}p$

Haidenbauer model [8] data have been used for primary $\bar{p}p$ -elastic scattering event generation. In Fig.2 the cross-section and the analysing power plots are presented for the three beam energies: 43, 120, and 220 MeV.

The **inverse transform method** has been used for $A_y(\vartheta)$ -dependent ϕ generation. The following cumulative distribution function is used:

$$F(\phi|\vartheta) \; = \; 1/\pi(\phi + QA_y(\vartheta)sin\phi), \tag{1}$$

with beam (or target) polarization $Q = 1$, and $\phi \in (0, \pm\pi)$. Other spin observables can be accounted in the same way. The generated event distributions for ϑ_{lab} and ϕ are shown in Fig.3.

inelastic interaction generation $\bar{p}p \to X$

For primary inelastic $\bar{p}p$ interaction generation CHIPS model has been used. The CHIPS model works only for $\bar{p}p$ hadronic interaction and is responsible for inelastic and charge-exchange interactions. The generated inelastic events are stored and later are used as primary event generator for simulation. The charge-exchange (and elastic) events generated by CHIPS model dicarded. Charge-exchange scattering events are generated separately.

In Table 2 we present the number of various types of particles generated in $\bar{p}p$ inelastic interactions corresponding to 1M primary interactions. Mainly $\pi^{\pm}$ and π^{o} are generated in

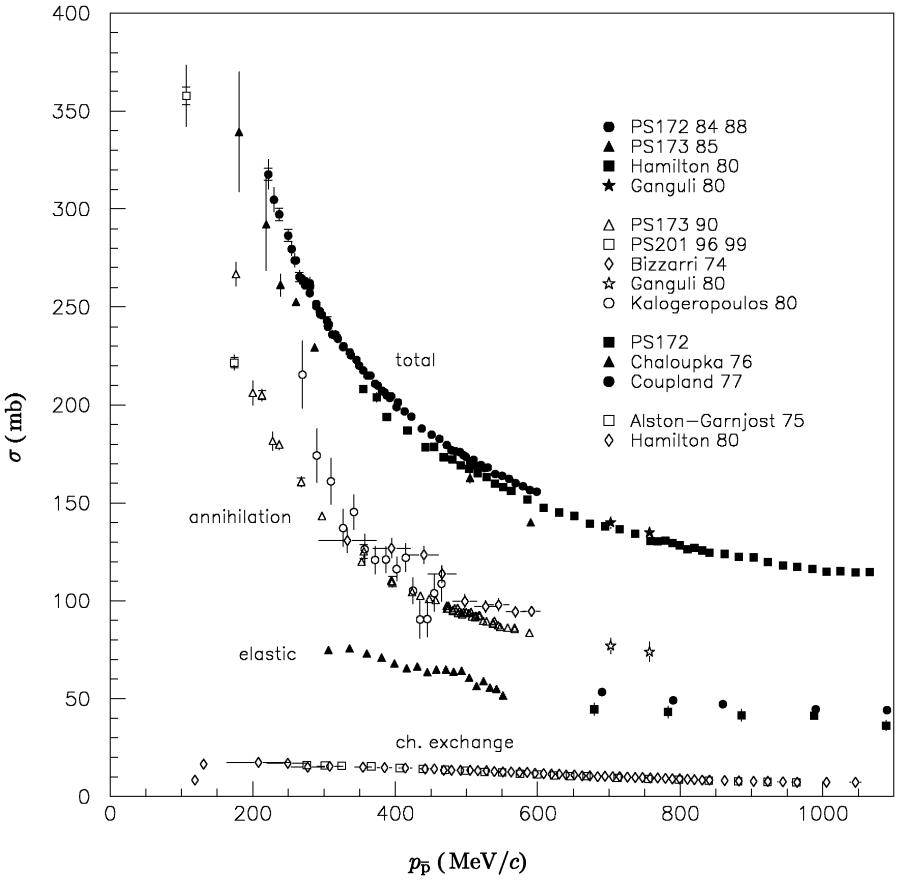

Figure 1. $\bar{p}p$ total cross section compillation from [6]

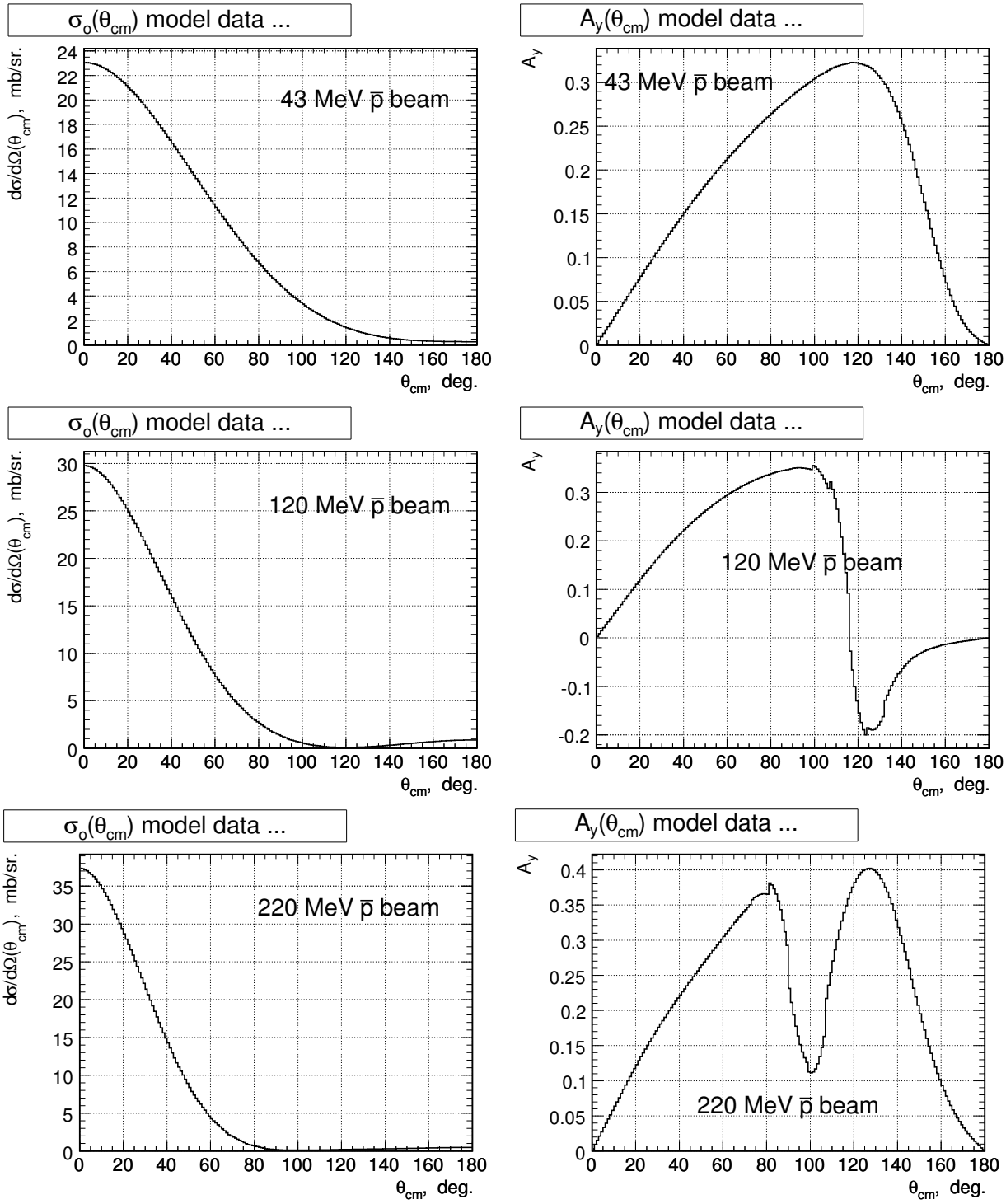

Figure 2. $\bar{p}p \to \bar{p}p$ -elastic scattering cross-sections and analysing powers at different energies. The model data.

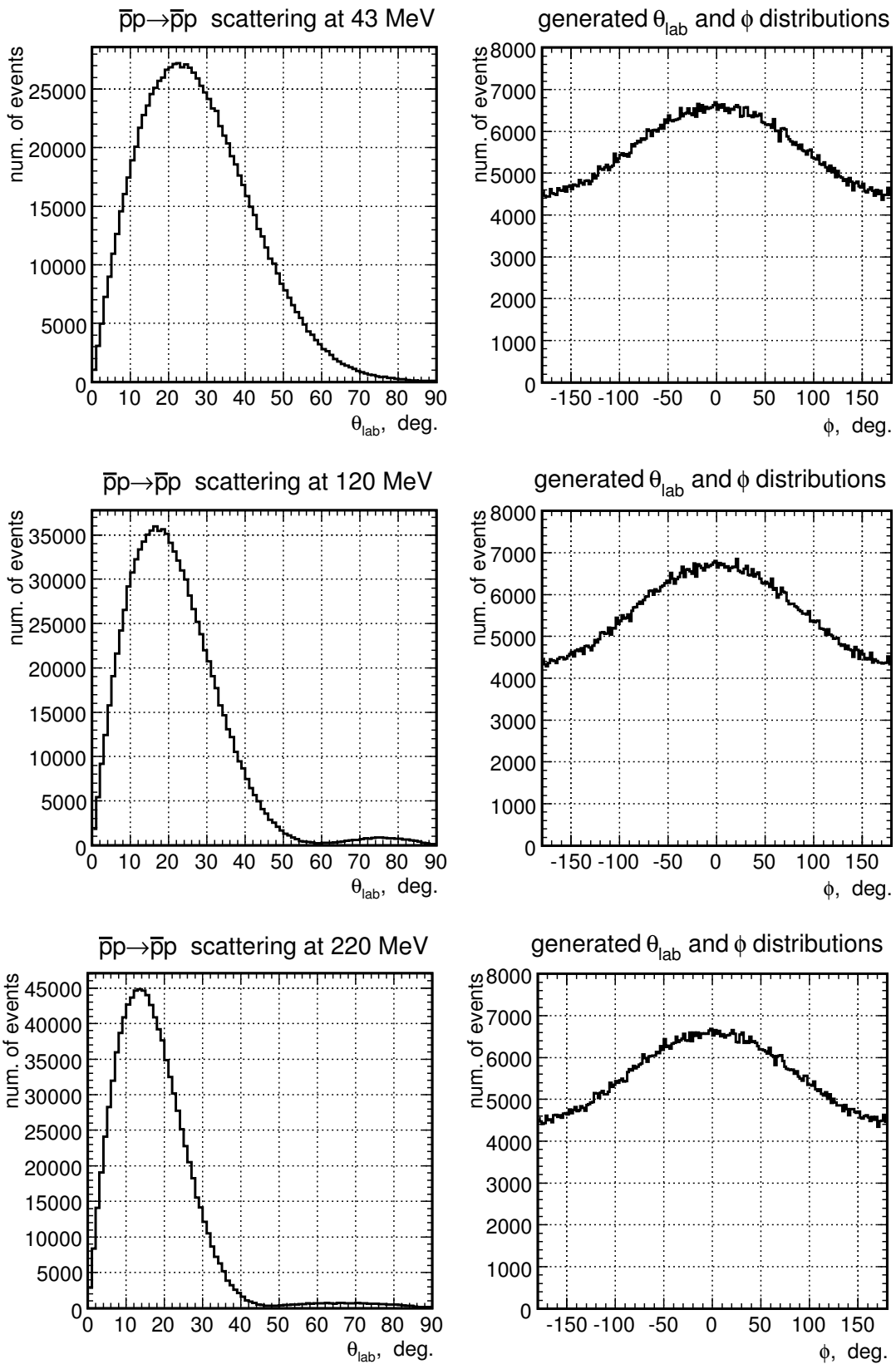

Figure 3. $\bar{p}p \to \bar{p}p$ -elastic scattering. The generated events distributions on ϑ_{lab} and ϕ at different energies.

$\bar{p}p \to X$ interaction (see Table 2). The distribution of number of secondaries produced in $\bar{p}p \to X$ -inelastic (or annihilation) interactions are shown in Fig.4 for all energies. The momentum spectra of all secondaries are independent on the antiproton beam energy (see Fig.5), so the detector operation conditions are the same for all energies.

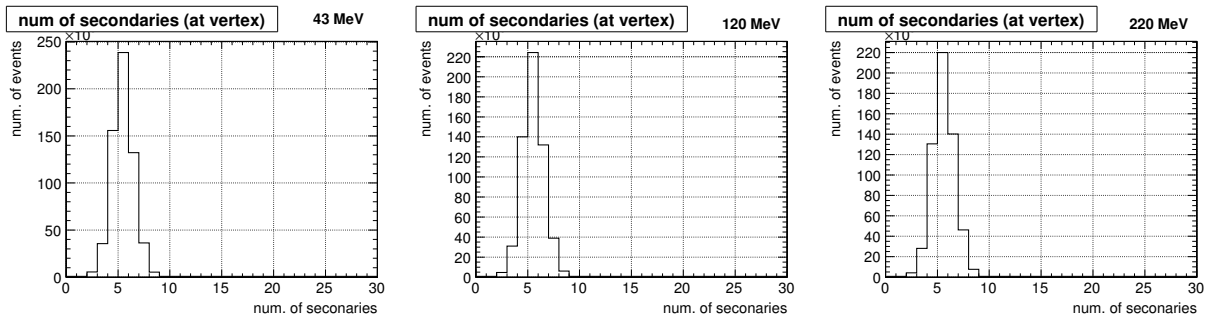

Figure 4. Number of secondary particles generated in inelastic interaction

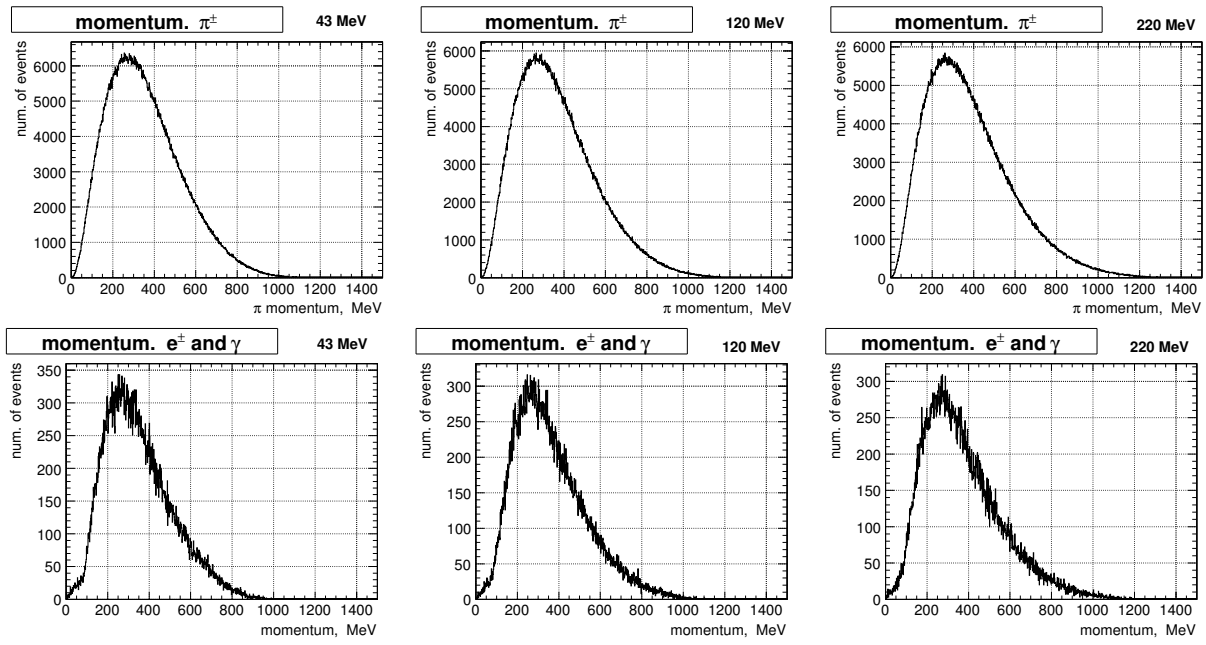

Figure 5. Momentum distributions of secondary $\pi^{\pm}$ (upper hists) and $e^{\pm}, \gamma$ (lower hists)

charge-exchange scattering generation $\bar{p}p \to \bar{n}n$

As was mentioned above, for charge-exchange scattering generation the experimental shape of charge-exchange cross-section (see Fig.6 from [6]) has been used. Experimental data from [6] is also used for $A_y^{\bar{p}p \to \bar{n}n}(\vartheta)$ accounting in the same way as for elastic scattering. In Fig.7 the generated ϑ_{lab} and ϕ distributions are shown. The charge-exchange scattering does not produce background. Nevertheless the events are passed to the transportation code.

interaction time generation

particle	$43\,MeV$	$120\,MeV$	$220\,MeV$
π^o	1056951	1010653	1023530
π^-	900406	863705	879190
π^+	900535	863695	879369
γ	76555	72346	73078
K^o	23425	22772	23511
$\bar{K}^o$	23296	22782	23332
K^-	21240	20768	21633
K^+	21111	20778	21454
e^-	728	677	657
e^+	728	677	657
n	17	23	18
$\bar{n}$	17	23	18
p	13	17	21
$\bar{p}$	13	17	21

Table 2. Number of generated particles in the primary inelastic interactions. The numbers correspond to 1M primary events (elastic, inelastic, charge-exchange)

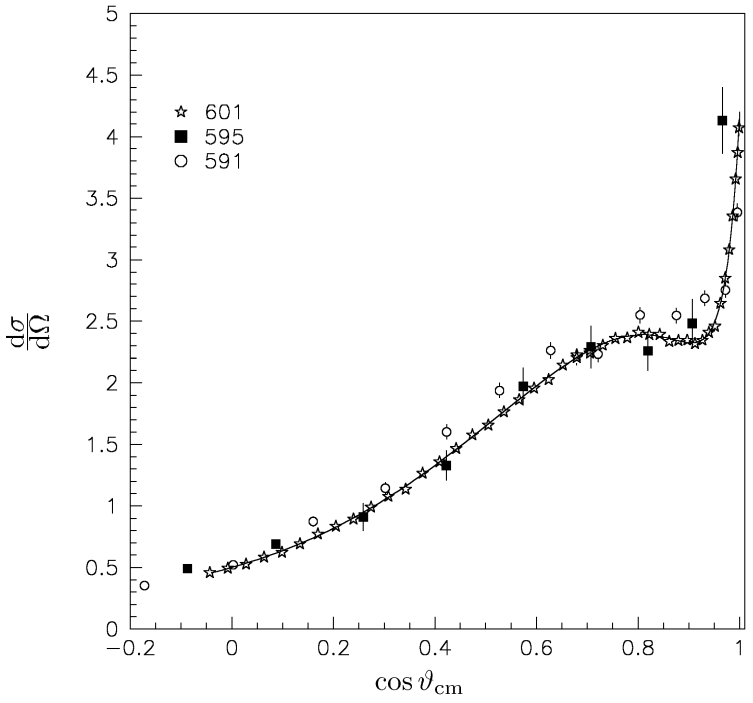

Figure 6. $\bar{p}p \to \bar{n}n$ charge-exchange scattering cross-section from [6].

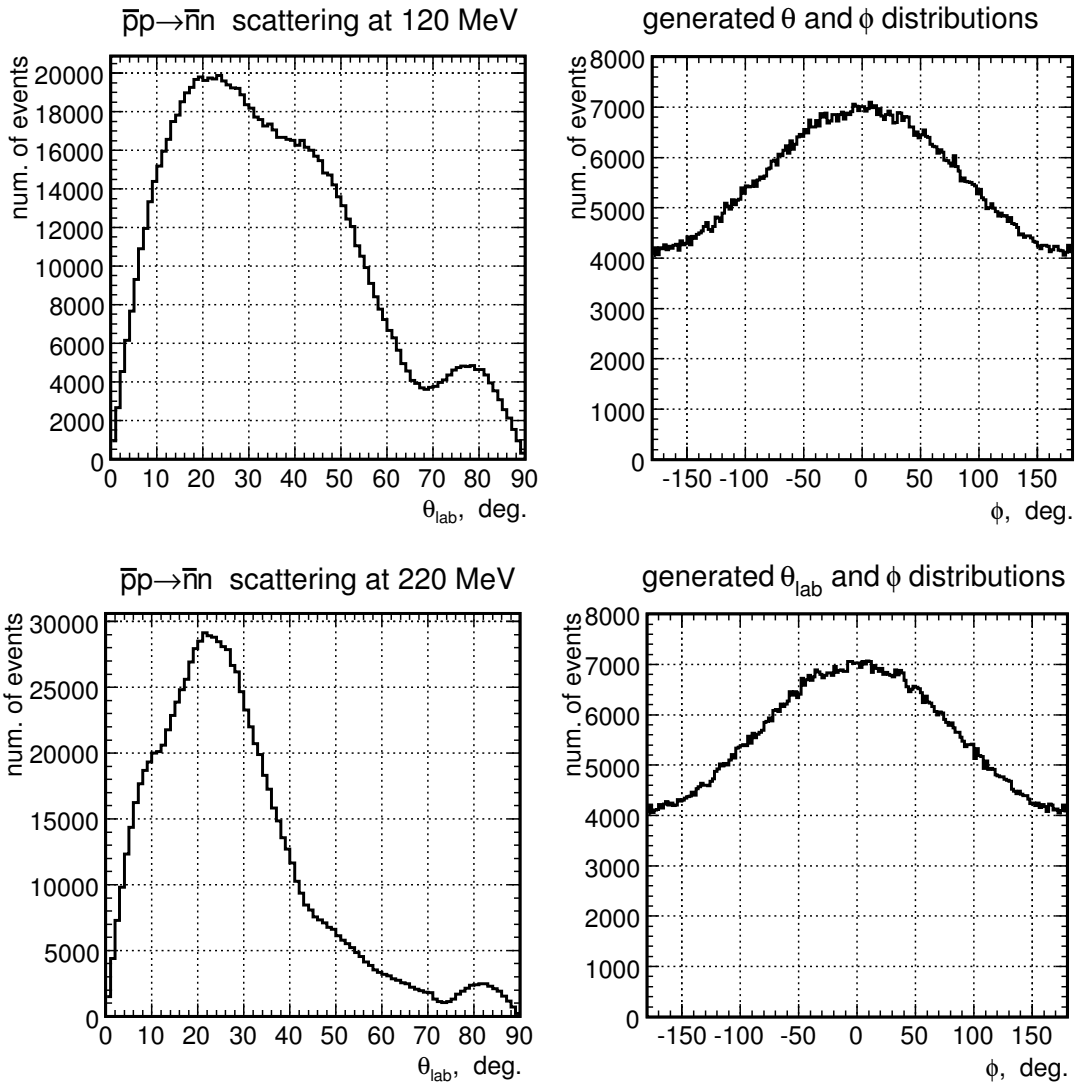

Figure 7. $\bar{p}p \to \bar{n}n$ -charge-exchange scattering. The generated events distributions on ϑ_{lab} and ϕ at different energies.

In the ANKE DAQ sream each event is identified by its sequential number, but also can be identified by the time stamp. The latter is essential for real experiment analysis. the timing data contains the absolute time in seconds (as it is defined in Unix-like systems) and microseconds. The time interval between events is defined by the luminosity and the total cross-section. The luminosity is taken constant and equals to $10^{27} cm^{-2} s^{-1}$ (AD) for all energies. The time interval between events is distributed according to the p.d.f.

$$\sim e^{-L\sigma_{tot}t}. \tag{2}$$

The total cross-sections at different energies are presented in Table 1 (see Fig.1 from [6]). The dead-time effect has not been applied. If necessary it can be accounted at the analysis stage by rejecting events with time interval less than dead-time (with corresponding smearing).

The event time generation makes possible to define events rate directly at the analysis.

3 Vertex generation

The vertex (interaction point) is generated randomly depending on the target gas density distribution function and the beam transverse sizes. In Fig.8 the generated interaction vertex coordinate distributions are shown.

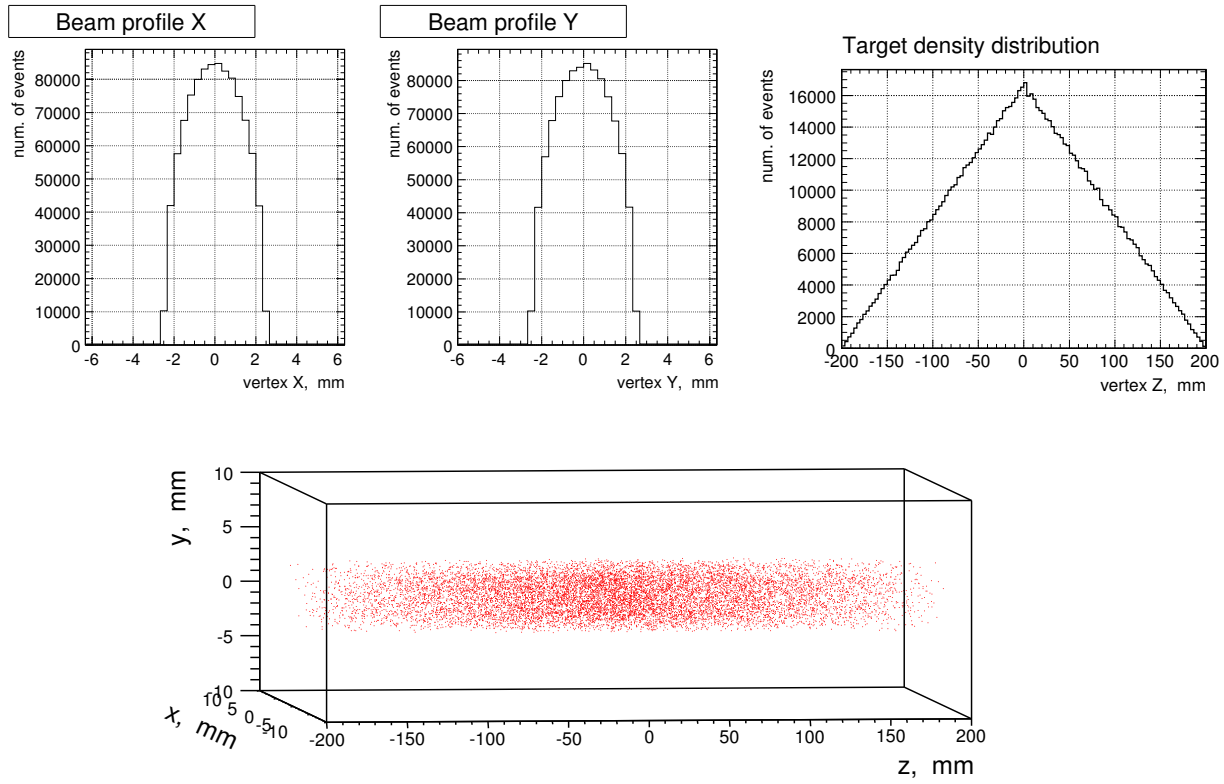

Figure 8. The generated vertex position distribution in the target.

4 Target description

target cell

target mechanical structures

energy depositions in mechanical parts of the target

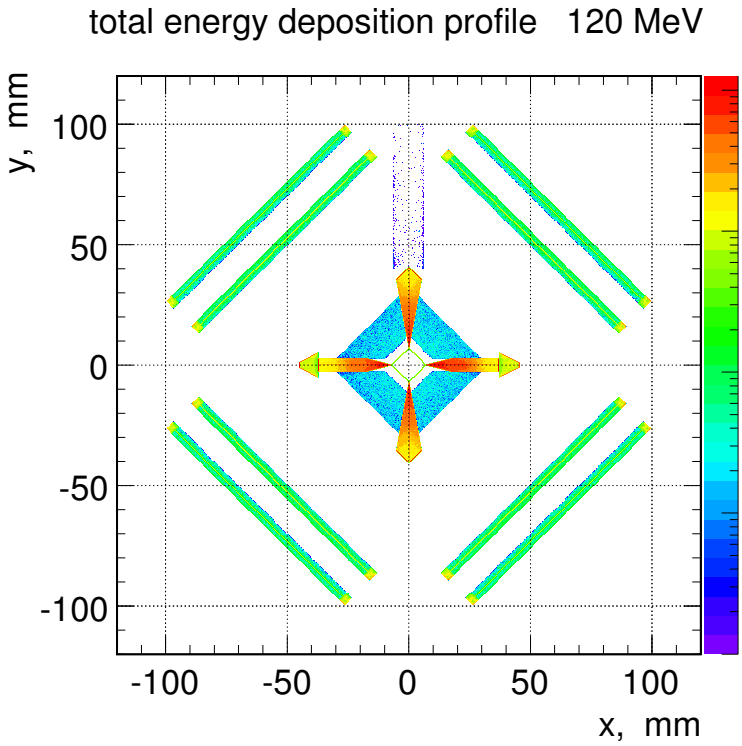

Figure 9. The deposited energy distribution in the detector mechanical parts. ANKE-type silicon modules are positioned closer to the cell.

Total energy deposition in the target and detector materials is shown in Fig.9. The distribution is almost the same for all beam energies.

5 Detector description

coordinate system

The right-handed cartesian coordinate system origin is placed at the target cell center, z -axis is directed along the beam, y -axis upwards. The system we call global detector system in contrast to the detector modules local systems.

The setup geometry is shown in Fig.10 (ANKE version) and in Fig.11 (HERMES version). The target is the same for both versions.

module geometry

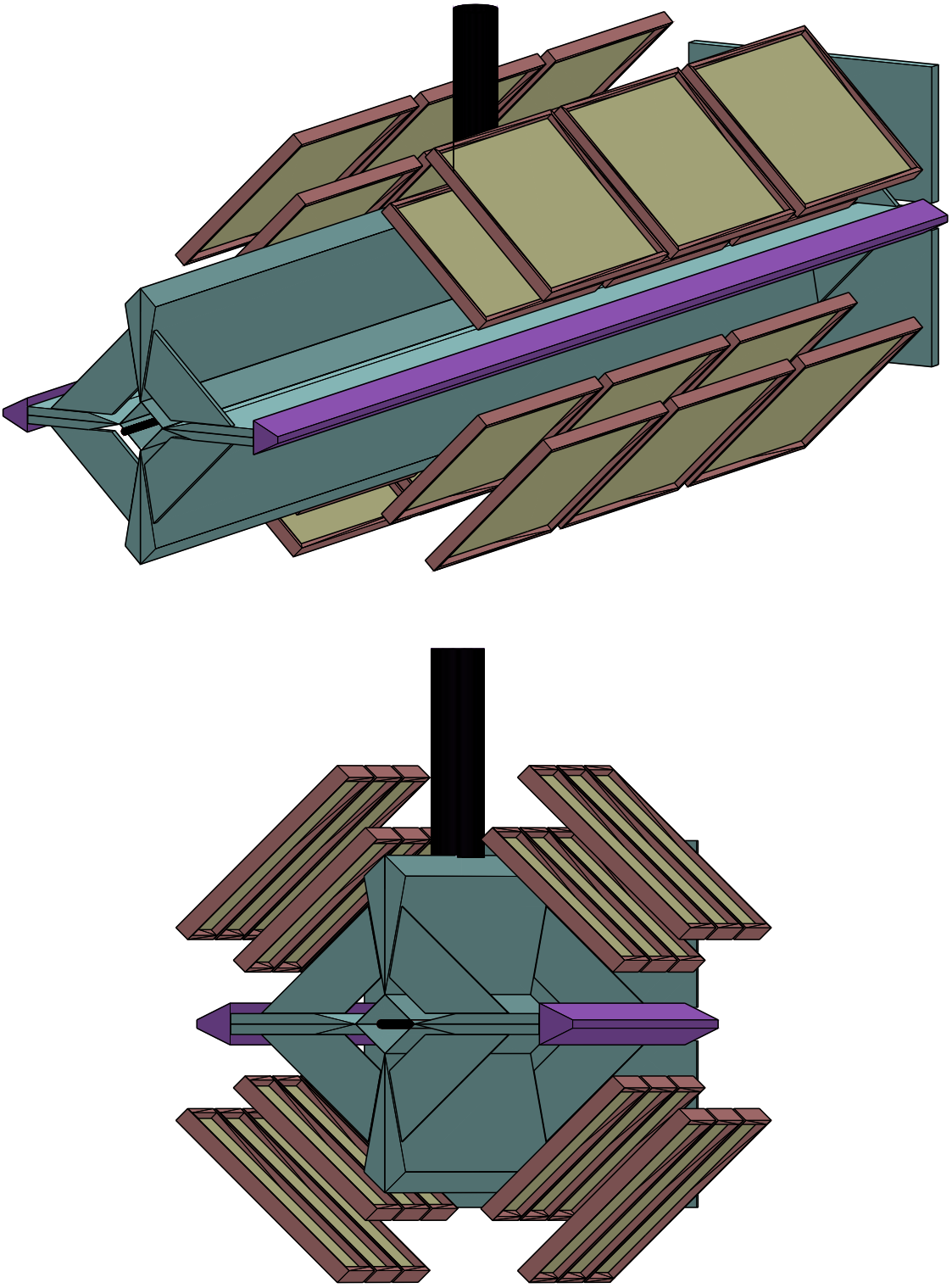

Figure 10. The detector with ANKE-type silicon modules.

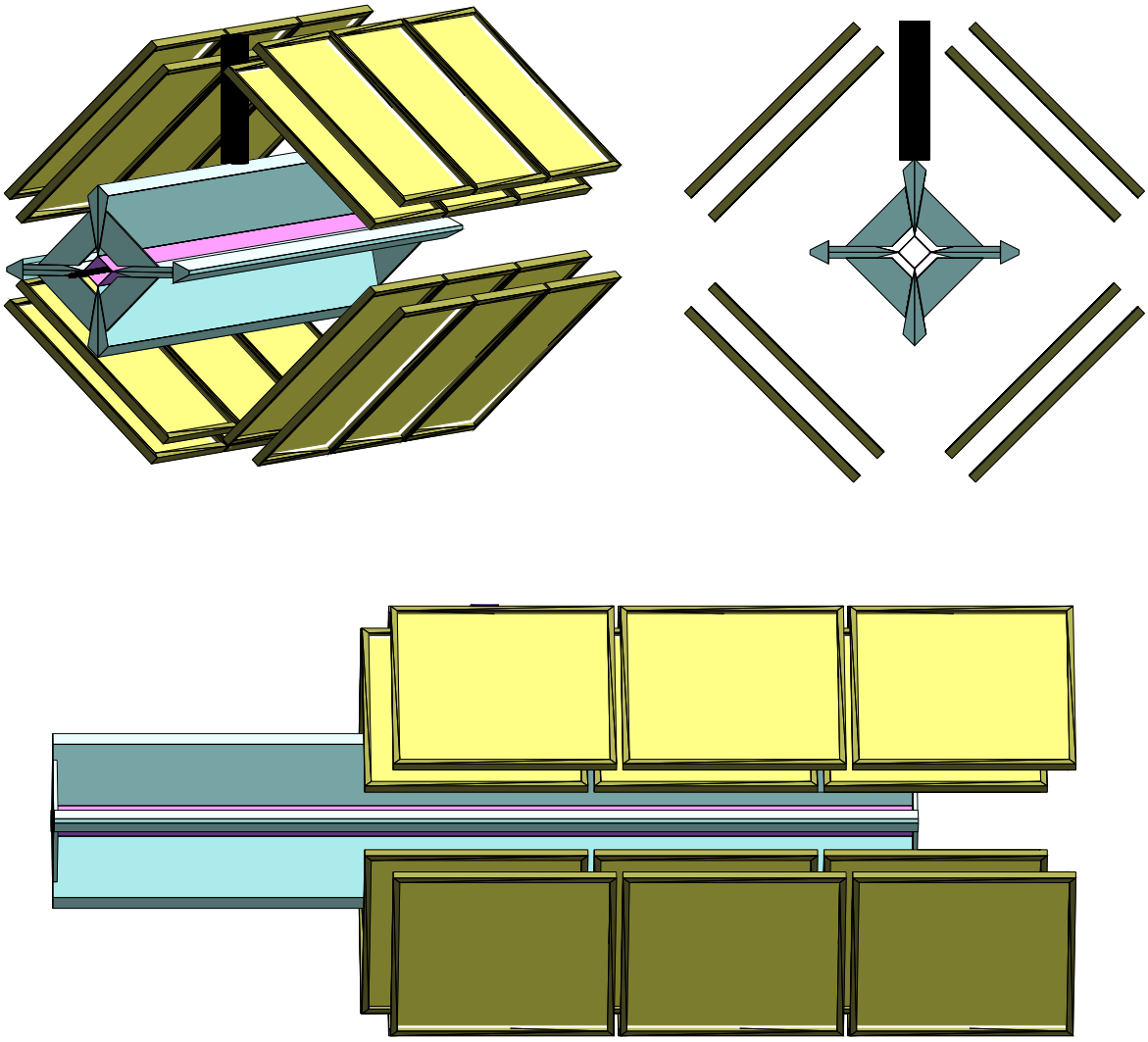

Figure 11. Detector setup with HERMES-type silicon modules. The target forward flange removed. The cell walls are shown in violet (Teflon), the target mechanical parts in sky blue (Aluminum), and the modules in yellow (Silicon).

parameter	unit	layer 1	layer 2
Active area	mm	97.3×97.3	97.3×97.3
Distance to beam axis	mm	72	87
layer thickness	μm	300	300
strip pitch (Δ_x, Δ_y)	mm	(0.758,0.758)	(0.758,0.758)
Frame cross-sect	mm	3×4	3×4
intermodule gap	mm	3	3
z_{min} position	mm	-60	-40

Table 3. The detector modules (HERMES-type) geometry and positioning.

The module parameters and positioning for HERMES version are shown in Table 3.

modules identification scheme

the sensitive module identifier consists of three components $id = \{l, t, s\}$.

l	layer	0 (closest to target), 1
t	telescope	0 (with lower z), 1, 2
s	sector	0 (with vector to module center $\phi = 45^o$), 1 (135^o), 2 (-135^o), 3 (-45^o)

optimized z positioning

z_{min} -position (see Table 3) has been chosen by iterations in order to get maximum possible overall acceptance. The second layer is shifted towards z -axis. Corresponding overall acceptances at all energies are presented in Table 7. If the second layer matches the first one without shift the acceptance somewhat drops[1].

6 Antiproton interaction with materials

GEANT4 contains the chiral invariant phase-space decay model (CHIPS) [7] which makes possible to simulate $\bar{p}$ annihilation in different materials. The model, recently added to the GEANT4 hadronic physics package, is well tested for $p\bar{p}$ annihilation using two-particle final state branchings. The CHIPS model is used for $\bar{p}p$ inelastic interaction and annihilation simulation.

ionization losses and multiple scattering

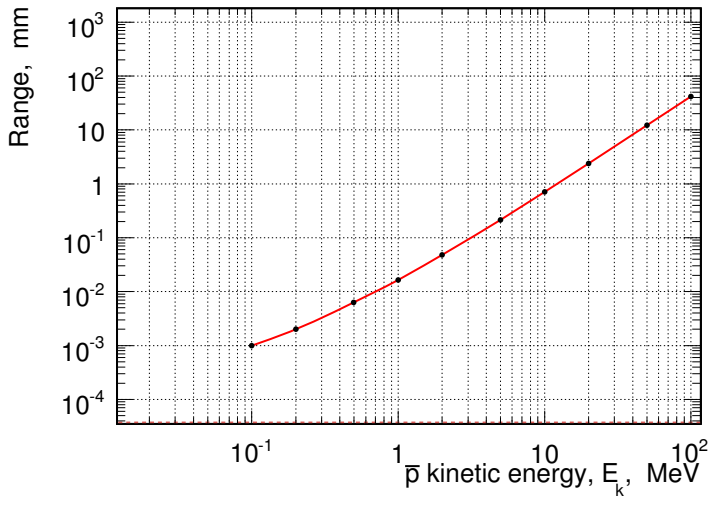

Figure 12. Energy dependence of antiproton range in silicon.

[1]Ralf noted that shifted second layer makes some mechanical problems. The acceptance in this case decreases (see Table 7) by 10 %. not so bad.

Electromagnetic interaction of antiprotons with material doesnot difer from that for protons. So, the ionization losses (energy deposits) and multiple coulomb scattering are the same. In Fig.12 the energy dependence of $\bar{p}$ range in silicon is shown.

num of steps	interaction type	interaction name
2124427	Transportation	Transportation
561827	Electromagnetic	hIoni
121	Electromagnetic	msc
5967	Hadronic	hElastic
4245	Hadronic	ProtonInelastic

Table 4. Proton interactions in materials.

num of steps	interaction type	interaction name
1882878	Transportation	Transportation
307249	Electromagnetic	hIoni
14	Electromagnetic	msc
27158	Hadronic	AntiProtonInelastic
17441	Hadronic	hElastic
23723	NotDefined	CHIPSNuclearAbsorptionAtRest

Table 5. Antiroton interactions in materials.

annihilation

The distribution of the number of the secondary particles produced in $\bar{p}$ annihilation is shown in Fig. 13(a). The distribution of the sum of the kinetic energies of all these secondaries, i.e. the energy which can potentially be deposited in a medium, is shown in Fig.13(b).

Antiproton annihilation position distribution in the setup is shown in Fig.14. The annihilation total rate (and rates in modules) are presented in Table 6.

beam energy	MeV	43	120	220
$\bar{p}$ annihilation rates				
total	%	16.4	6.7	0.70
layer 0	%	0.74	0.40	0.15
layer 1	%	0.72	0.15	0.06

Table 6. Antiroton annihilation rates at different energies.

$\bar{p}$ and p hadronic interactions

Proton and antiproton hadronic interaction in materials are shown in Fig.15 and 16. Lists of all interactions of protons and antiprotons with materials are shown in Tables 4 and 5.

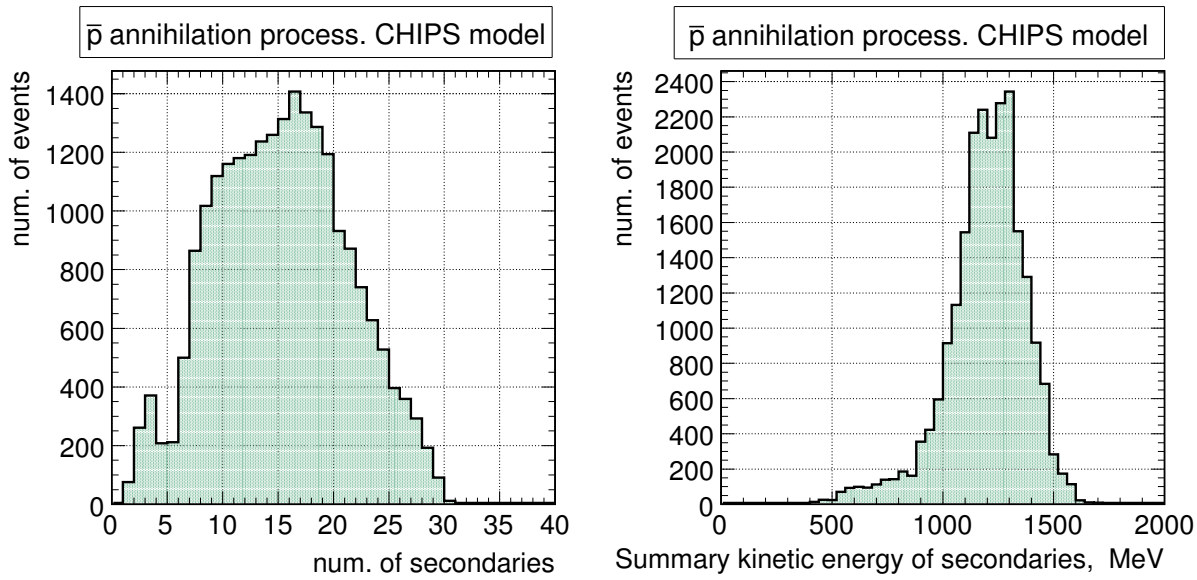

Figure 13. (a) Number of secondaries in $\bar{p}$ annihilation; (b) Sum of kinetic energies of secondaries.

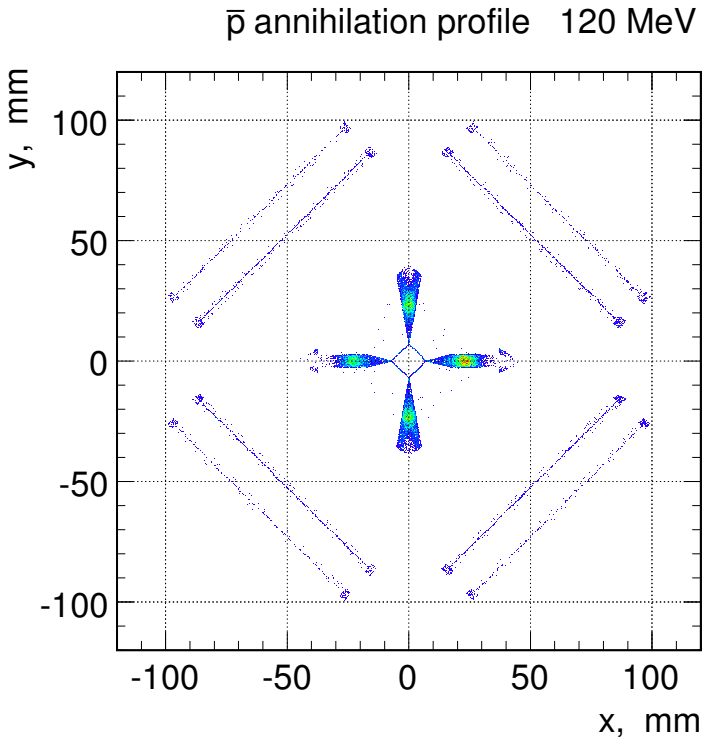

Figure 14. Antiproton annihilation point distribution in the detector with HERMES-type modules.

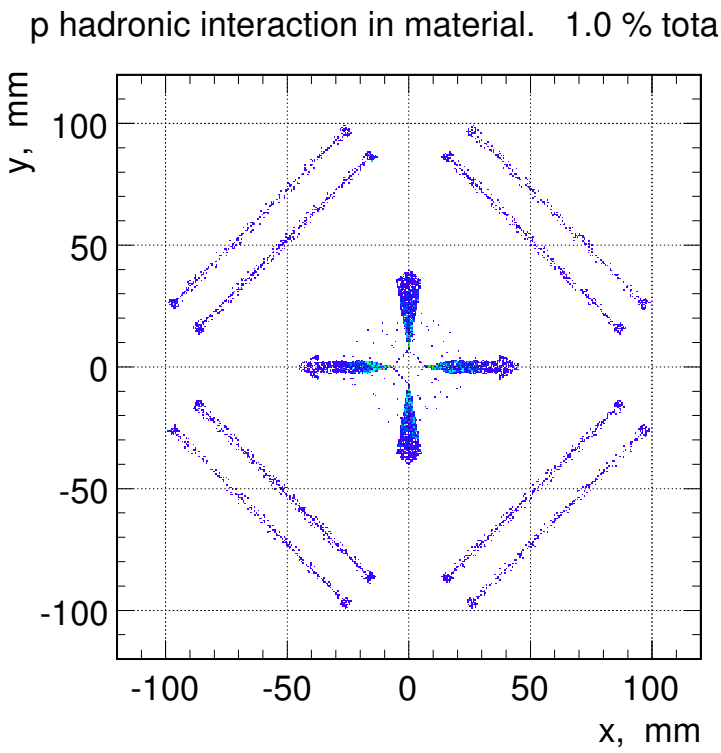

Figure 15. Proton hadronic interaction point distribution in the detector with HERMES-type modules.

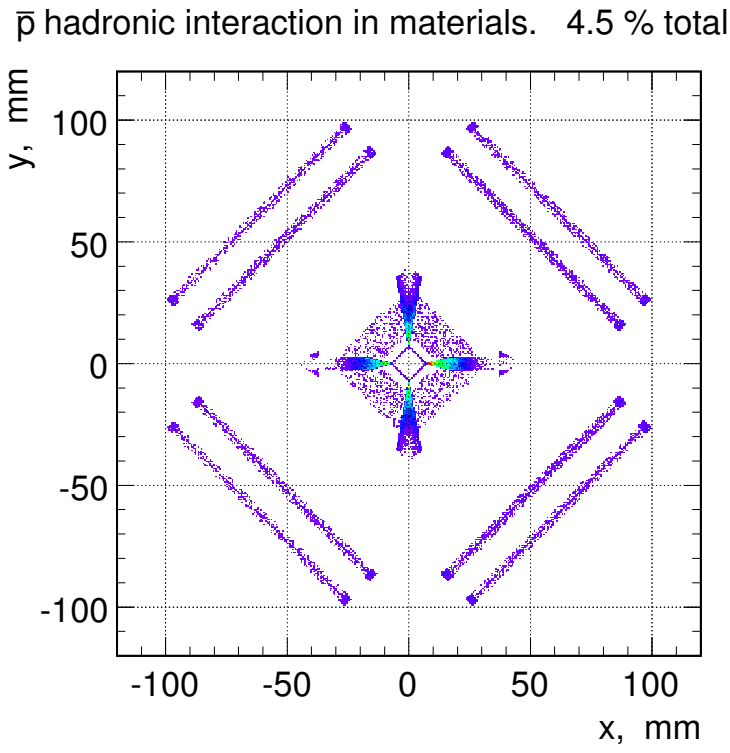

Figure 16. Antiproton hadronic interaction point distribution in the detector with HERMES-type modules.

7 Energy deposits in sensitive modules

In Fig.17 and 18 the energy depositions are shown for all events. Lower amplitude signals correspond to the background energy deposits (mainly pions). Only first layer data are shown, second layer (also of $300\,\mu m$ thichness) response is almost the same. Fig.18 shows clearly firs layer modules positions along the target.

8 Time measurement

The cluster time distributions are shown in Fig.21 for 120 and 220 MeV beam energies. In real experiment we only can measure time differences. It seems that the time difference measurement uncertainty is not sufficient to use in event selection.

9 Event reconstruction

Most important reaction parameters (kinematicaly independent) are ϕ_n - the reaction plane normal, and ϑ - the scattering angle. Reliable and precise reconstruction of these parameters in each event makes possible to measure any spin observable using the beam and the target of appropriate directions of polarization. The reaction plane reconstruction algorithm has been developed in order to define the expected uncertainties caused by the multiple scattering and the energy losses. The reaction plane is reconstructed using 3D -coordinates of 4 geometricaly selected clusters (two in each layer). The plane is built with a severe constraints, to be parallel to the beam axis (z), and minimum distance to z axis to be less than the beam radius. The reconstruction algorithm is based on the *orthogonal regression method* providing a parameter characterizing 'goodness of fit' (χ^2). After the plane is reconstructed successfuly, the 3D coordinates of the selected clusters are transformed to the 2D system in the reconstructed plane coordinate system. Assuming that the beam is parallel to the z axis, and varying the coordinates of the plane tracks, the scattering and the recoil angles are adjusted to each other.

...other versions ...

... $A_y(\vartheta)$ reconstructed ...

10 Acceptance and event rate estimate

AD luminosity is taken equal to $10^{27} cm^{-2} s^{-1} = 1 mb^{-1} s^{-1}$ at all energies. The integral acceptance data are collected in Table 7. In Fig. 22 the acceptance is shown as a function of vertex z -coordinate at 120 MeV beam energy. The triangular distribution corresponds to all primary generated events.

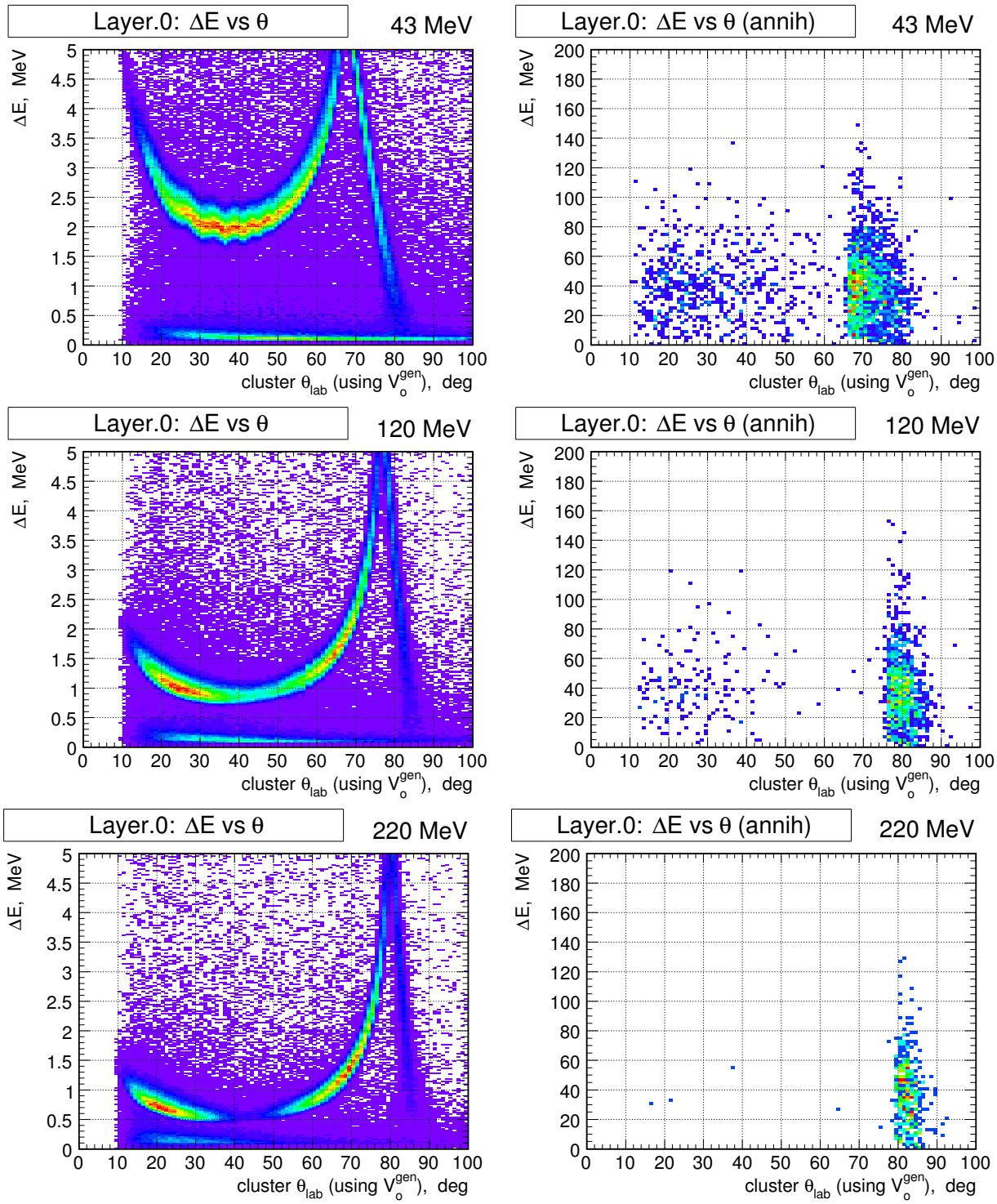

Figure 17. Energy depositions vs θ without annihilation (left column) and with $\bar{p}$ annihilation (right column) in the first layer at beam energies: (a) 43 MeV, (b) 120 MeV, (c) 220 MeV (from top to bottom). Lower amplitude signals correspond to pion energy deposits. Only elastic events are included. **Note:** the detector intrinsic resolution is not applied to the deposited energy signal.

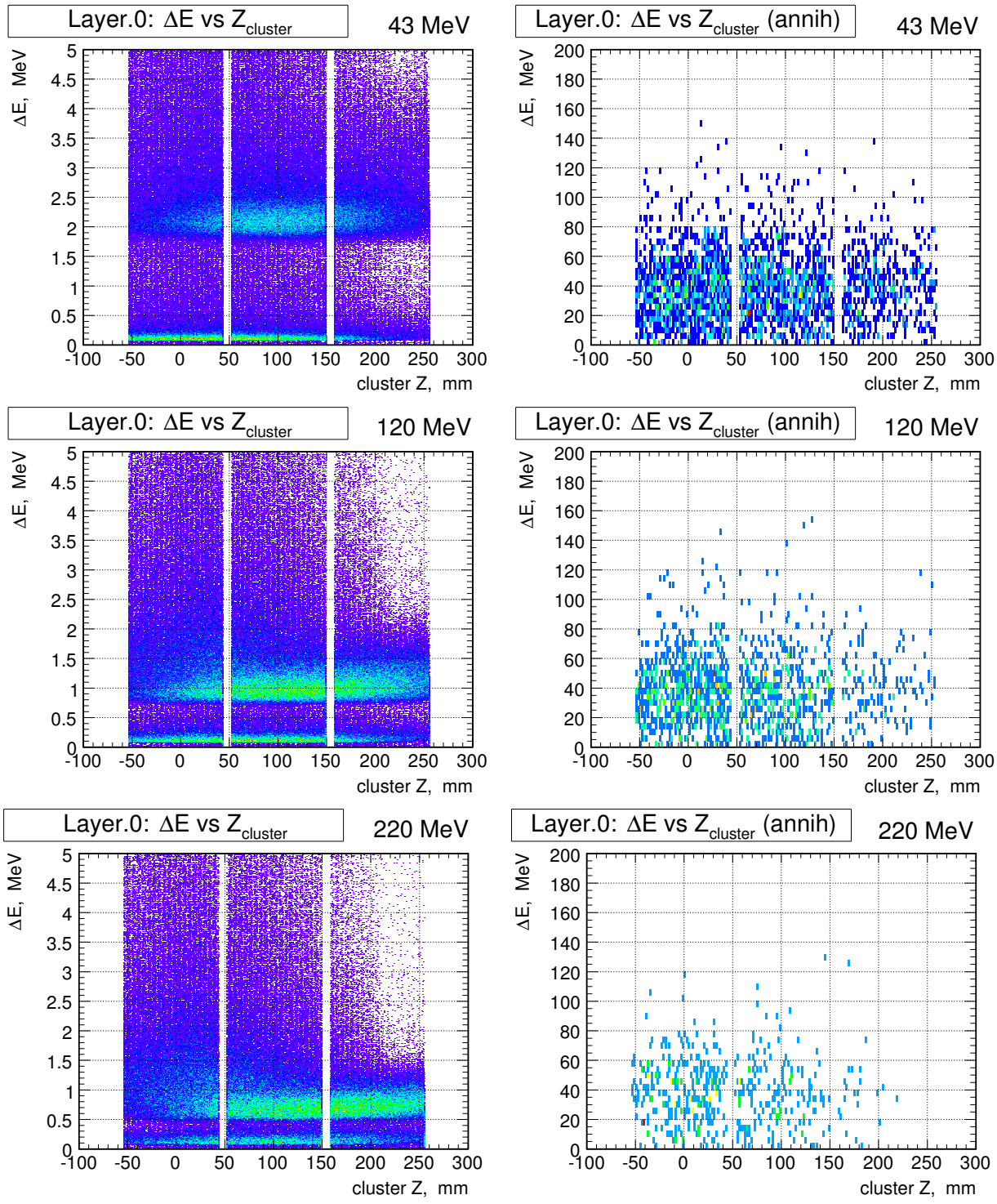

Figure 18. Energy depositions vs z coordinate without annihilation (left column) and with $\bar{p}$ annihilation (right column) in the first layer at beam energies: (a) 43 MeV, (b) 120 MeV, (c) 220 MeV (from top to bottom). Lower amplitude signals correspond to pion energy deposits. Only elastic events are included. **Note:** the detector intrinsic resolution is not applied to the deposited energy signal.

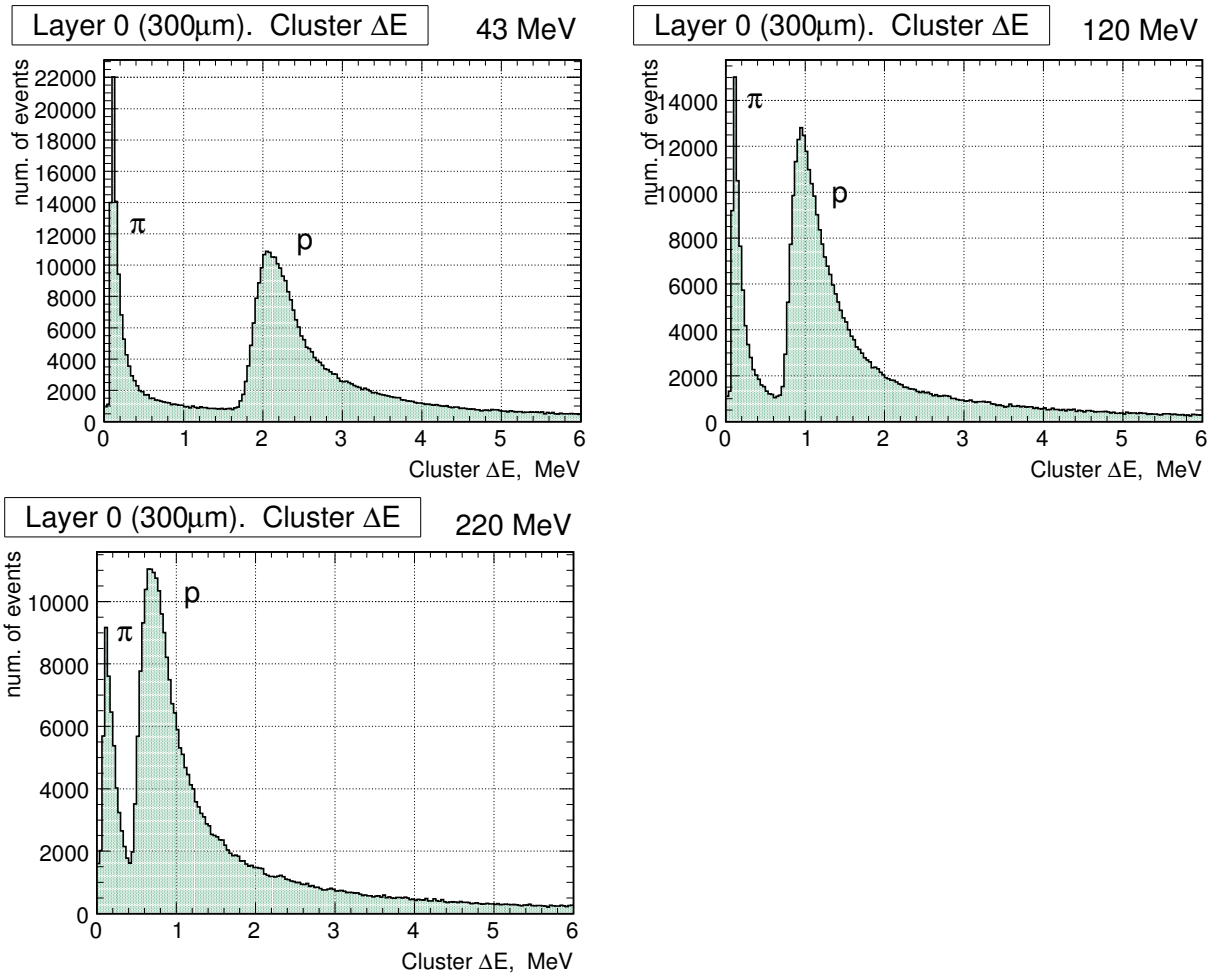

Figure 19. Energy depositions in the first layer at beam energies: 43, 120, and 220 MeV. Lower amplitude signals correspond to pion energy deposits. Only the primary elastic events are included. **Note:** the detector intrinsic resolution is not applied to the deposited energy signal.

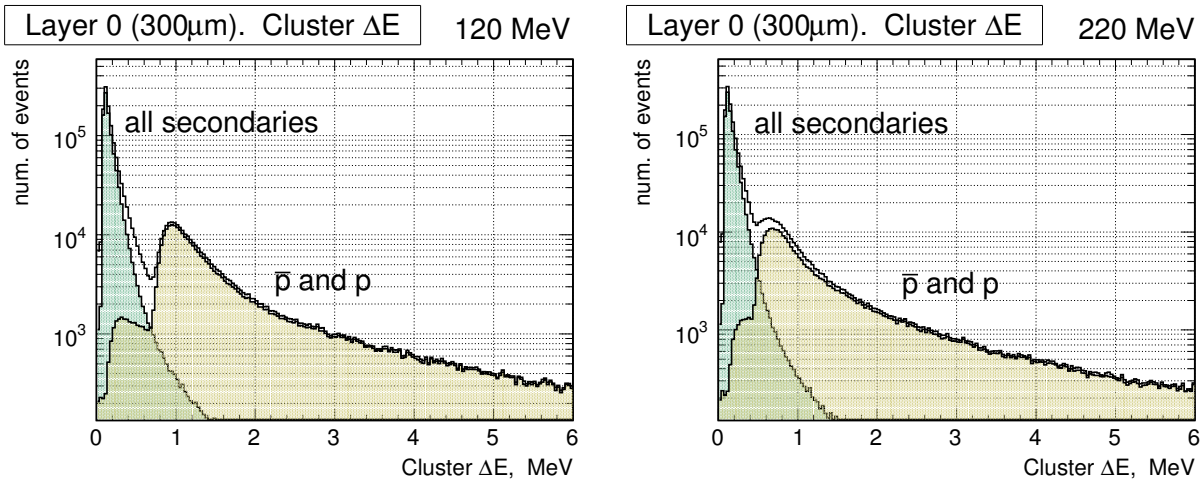

Figure 20. Energy depositions in the first layer at beam energies: 120, and 220 MeV. Lower amplitude signals correspond to pion energy deposits. All the primary events are included. **Note:** the detector intrinsic resolution is not applied to the deposited energy signal.

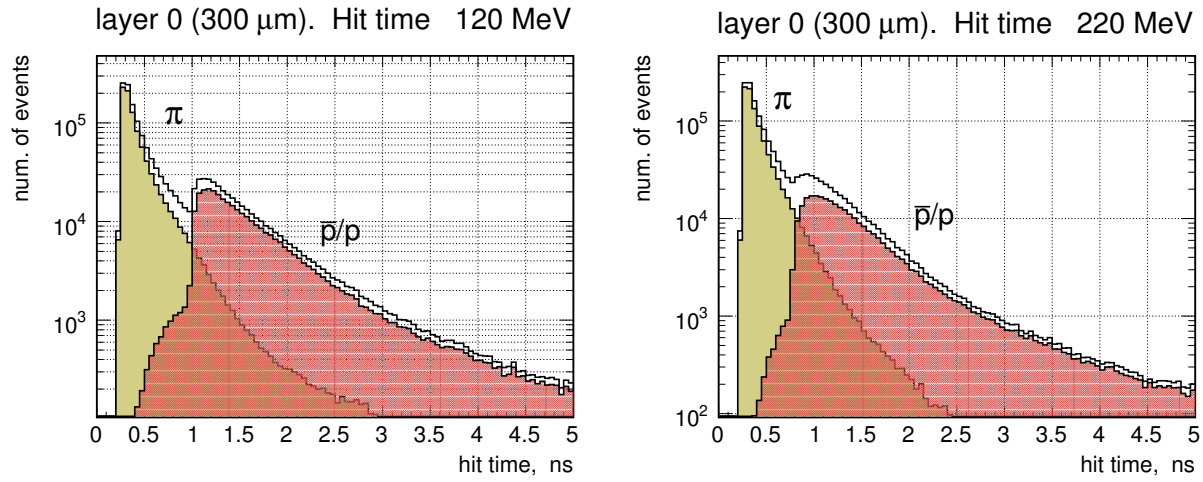

Figure 21. Cluster time measurement in the first layer at beam energies: 120, and 220 MeV. All the primary events are included. **Note:** the detector intrinsic resolution is not applied to the hit time.

$\bar{p}$ and p mixing effect

In Fig. 23 the measured ϑ_{lab} -dependent acceptance is shown. If we ignore $\bar{p}$ annihilation it is impossible to distinguish between $\bar{p}$ and p. So we are forced to consider a track with smaller scattering angle as forward particle (in c.m. system), like in case of $pp \to pp$ elastic scattering. This leads to $\bar{p}/p$ mixing effect. In Fig. 23 antiprotons with $\vartheta_{lab} > 45^o$ are accepted as recoil protons, so the accepted ϑ_{lab} distribution is degenerated. But the $\bar{p}p$ elastic scattering cross-section ϑ dependence above 120 MeV is favorable and almost eliminates the mixing effect. In any case the existing experimental data on $\bar{p}p$ elastic scattering cross-section and analysing power (see [6]) makes possible to account correctly the influence of the mixing effect.

parameter	unit	$43\,MeV$	$120\,MeV$	$220\,MeV$
total number of primary events		1 M	1 M	1 M
$\bar{p}p \to \bar{p}p$ -primary		0.33 M	0.33 M	0.33 M
$\bar{p}p \to \bar{p}p$ -accepted		48 k	56k	40 k
	% ($\bar{p}p \to X$)	4.8	5.6	4.0
2nd layer not shifted	% ($\bar{p}p \to X$)	-	5.2	-
	% ($\bar{p}p \to \bar{p}p$)	14.5	17.0	12.0
total 'run' time	sec	4000	5700	6898
reconstructed event rate	evt/sec	12	10	5.8
'accepted' backgound events	%	0	0	0
$\bar{p}$ annihilation rate	% ($\bar{p}p \to \bar{p}p$)			
total		16.4	6.7	0.70
layer 0		0.74	0.40	0.15
layer 1		0.72	0.15	0.06

Table 7. Integral acceptances and rates at three energies: 43, 120, and 220 MeV. AD luminosity is taken equal to $10^{27} cm^{-2} s{-}1 = 1 mb^{-1} s^{-1}$. Corresponds to the geometry described in Table 3.

11 Measurement uncertainties

Almost no difference in the detector performance has been detected between the two versions of strip pitch (0.5 and 0.758 mm, see Table 11). multiple scattering dominates at energies around 120 MeV. The measured parameter uncertainties for these two versions are shown in Table 11.

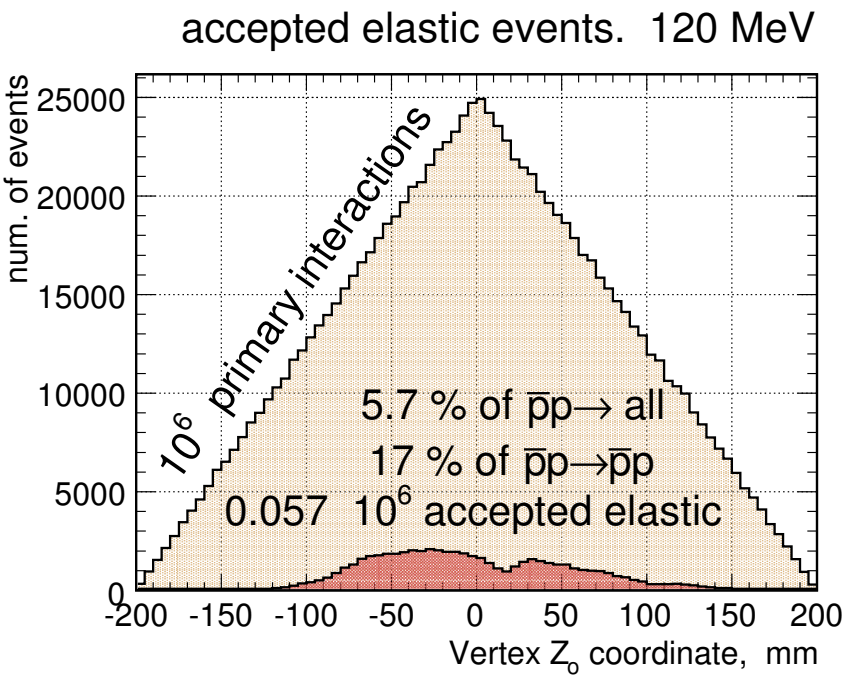

Figure 22. Accepted (reconstructed) events distribution on vertex z coordinate at 120 MeV.

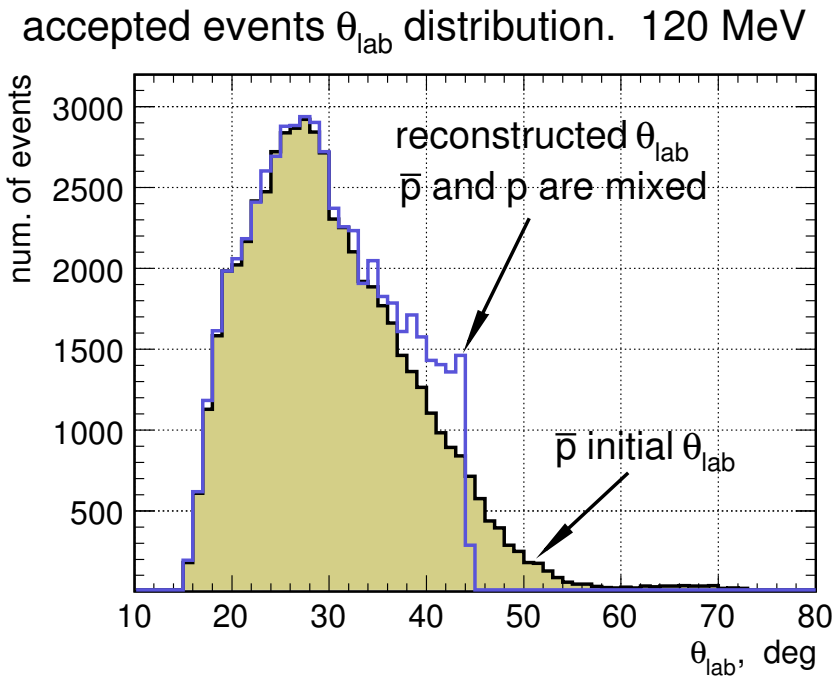

Figure 23. Accepted (reconstructed) events distribution on ϑ_{lab} scattering angle at 120 MeV. All the primary events are included.

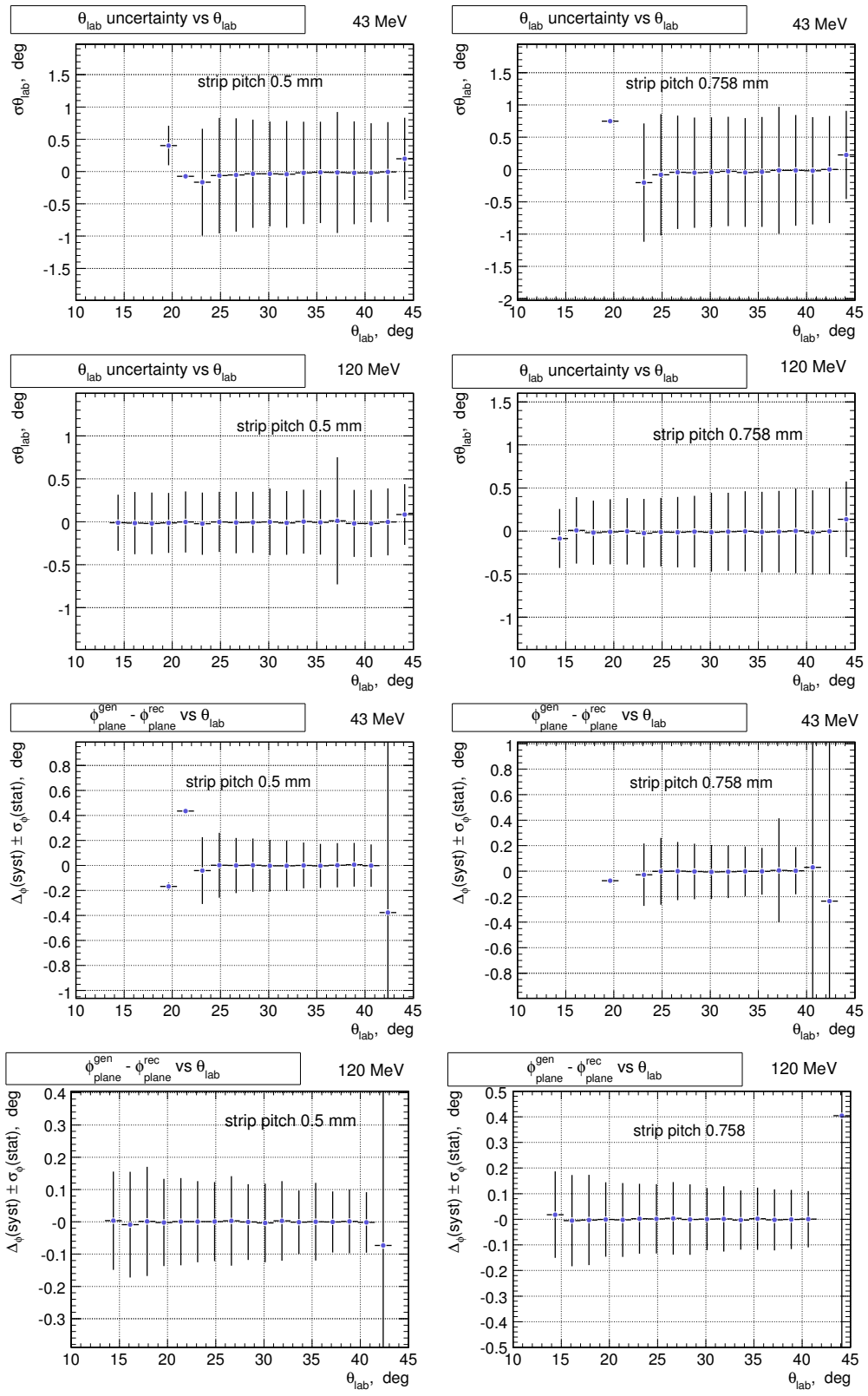

Figure 24. ϑ_{lab} and ϕ_{plane} uncertainties vs ϑ_{lab} with 0.5 and 0.758 strip pitch. HERMES-type modules. Some inhomogenous behaviour of ϕ_{plane} uncertainty above 42^o is caused by mixing of scattered and recoil particles. In ϕ measurement profile the unceratinty at $\vartheta_{lab} > 40^o$ can not be defined correctly due to the mixing effect. The reaction plane normal sometimes is defined in the opposite direction.

strip pitch	mm	$0.5\,mm$			$0.758\,mm$		
beam energy	MeV	43	120	220	43	120	220
$\sigma\vartheta_{lab}$	deg	0.77	0.35	0.25	0.81	0.42	0.32
$\sigma\phi$	deg	0.26	0.16	0.12	0.27	0.18	0.14
vertex $\sigma_x = \sigma_y$	mm	1.90	1.35	1.20	2.05	1.47	1.35
vertex σ_z	mm	0.34	0.19	0.14	0.35	0.21	0.17

Table 8. Parameter uncertainties depending on strip pitch.

12 Conclusions

- The same detector can be used for measurements at COSY and AD, perhaps with minor modifications;
- About 10 reconstructed $\bar{p} \rightarrow \bar{p}p$ elastic events can be accepted at 120 MeV beam energy.
- Antiproton annihilation in the target environment as well as in the detector materials does not produce significant background. Annihilation rate in silicon does not exceed 0.7 %;
- Antiproton primary inelastic interaction background does not depend on the beam energy and can be eliminated with proper selection criteria;
- Elastic scattering reconstruction in pp and $\bar{p}p$ interactions does not differ. Annihilation events can be ignored. If we ignore $\bar{p}$ annihilation it is no way to distinguish between $\bar{p}$ and p tracks;
- No principal difference in performance in case of strip pitch 0.5 or 0.76 mm (HERMES-type) at 120 MeV.
- Preferable beam energy is around 120 MeV (or somewhat above) - good π/p separation by ΔE, $\sigma^{el}_{\bar{p}p}(\vartheta)$ and $A_y(\vartheta)$ favorable shapes (forward $\bar{p}$ dominates), less annihilation rate, less track spread due to MS;
- In all calculations the detector intrinsic resolutions (on ΔE and time measurements) were not accounted.

13 Open questions

- There are performance parameters that can only be checked and validated through actual testing with beam (e.g. intrinsic resolution, elsectronics noise, etc.). These parameters have to be accounted at the detector response (clusters) simulation.

- Antiprotons can be identified using degrader and measure the annihilation signal (large enough in comparison with ionization losses). The method has to be tested for applicability and efficiency.
- Persistent event structure and access methods have to be developed.
- Data base structures/interfaces have to be developed,
- Trigger logic has to be added in the simulation chain.
- Time differences should be checked in order to decide whether they can be used for analysis.

14 Geant4 specific details

software

Compillator version:	`g++ 4.1.0`
Platform:	**x86_64-suse-linux (10.1)**
Geant4 source code:	`geant4.8.p02`
Libraries	`clhep-2.0.3.1`
	`SoXT-1.2.2`
	`Coin-2.4.5`
	`dawn-3.88a`
Databases	G4ELASTIC.1.1
	G4EMLOW.4.0
	G4NDL.3.9
	PhotonEvaporation.2.0
	RadiativeDecay.3.0
Complete PhysicsList	QGSP
Test	Ex02PhysicsList
DefaultCutValue	$0.2\,mm$

Table 9. Geant4 environment.

materials

The materials used in the simulation program are shown in Table 10. Currently we use [1]Vacuum, Teflon, Aluminum, and Silicon.

volumes

physics lists

The physics list responsible for particle interaction with medium, contains several processes. All these processes are listed in Table 12. Steps means the number of steps defined by the corresponding process.

Material	Elem.	Z	$A\,g/mole$	fraction	density, g/cm^3
[1]Vacuum(air)	N	7	14.007	0.7494	$10^{-4}\,Pa/10^{-9}\,bar$
	O	8	15.999	0.2369	
	Ar	18	39.948	0.0129	
	H	1	1.008	0.0008	
[2]Vacuum(air)	same				$10^{-1}\,Pa/10^{-6}\,bar$
Teflon (CF_2)	C	6	12.011	1a	2.20
	F	9	18.998	2a	
Silicon	Si	14	28.090	1.0	2.33
Aluminum	Al	13	26.980	1.0	2.70
Aluminum dioxide Al_2O_3	Al	13	26.980	2.0	3.97
	O	8	15.999	3.0	
Stainless steel	Fe	26	55.845	0.6996	8.02
	C	6	12.011	0.0004	
	Mn	25	54.938	0.0100	
	Cr	24	51.996	0.1900	
	Ni	28	58.693	0.1000	

Table 10. List of materials.

Particle	PDG code	number	Name (G4)
p	2212	56067	proton
$\bar{p}$	-2212	94325	anti_proton
γ	22	75754	gamma
$d-Si$	0	35087	GenericIons
π^o	111	14596	pi0
π^+	211	26508	pi+
e^-	11	8676	e-
π^-	-211	19475	pi-
e^+	-11	1603	e+
K^+	321	548	kaon+
K^o_S	310	314	kaon0S
K^-	-321	232	kaon-
K^o_L	130	546	kaon0L
μ^+	-13	105	mu+
Λ	3122	62	lambda
Σ^+	3222	2	sigma+
μ^-	13	23	mu-
Σ^-	3112	1	sigma-

Table 11. List of particles produced at $\bar{p}$ annihilation in silicon detector of $5\,mm$ thickness. The numbers of the generated particles correspond to 10^5 initial antiproton events. Total number of $\bar{p}$ annihilations is equal to $0.61 \cdot 10^5$.

Steps	Proecess name (Geant4)
132229	idle step
1257003	msc
474371	Transportation
45945	hIoni
24523	ionIoni
14665	Decay
8747	CHIPSNuclearAbsorptionAtRest
3859	eIoni
1262	eBrem
998	hElastic
611	AntiProtonInelastic
259	conv
236	phot
152	compt
87	ProtonInelastic
70	PionMinusInelastic
61	PionPlusInelastic
42	muIoni
34	DeuteronInelastic
20	AlphaInelastic
20	TritonInelastic
10	annihil
9	KaonZeroLInelastic
3	KaonMinusInelastic

Table 12. Partial frequences (weights) of all physics processes in silicon detector. Physics list `QGSP` is used. Steps means the number of steps defined by the corresponding process.

References

[1] PAX Collaboration. Measurement of the spin-dependence of the $\bar{p}p$ interaction at the AD-ring. Jülich, 2005. **http://www.fz-juelich.de/ikp/pax/**

[2] A. Kacharava *et al.*, *Spin Physics from COSY to FAIR*. 2005. **http://www.fz-juelich.de/ikp/anke/**

[3] *Spin-Filtering Studies at COSY*, 2006, **http://www.fz-juelich.de/ikp/pax**.

[4] *Measurement of the Spin-Dependence of the $\bar{p}p$ Interaction at the AD-Ring*, 2005 **http://www.fz-juelich.de/ikp/pax**.

[5] Technical Proposal. *Antiproton-Proton Experiments with Polarization*, PAX Proposal, **arXiv:hep-ex/0505054**

[6] E.Klempt et al., Phys. Rep. **368** (2002) 119
E.Klempt et al., **arXiv:hep-ex/0501020v1**

[7] J.P. Wellish., **ePrint: nucl-th/0306006**

[8] V.Mull, K.Holinde. Phys. Rev., **C 51** (1995) 2360,
J. Haidenbauer *et al.*, Phys. Rev., **C 45** (1992) 952,
T.Hippchen *et al.*, Phys. Rev., **C 44** (1991) 1323